Research Article Vol. 7, No. 12 / December 2020 / *Optica* 1805

optica

Inverse-designed photon extractors for optically addressable defect qubits

SRIVATSA CHAKRAVARTHI,[1,†,*] PENGNING CHAO,[2,5,†] CHRISTIAN PEDERSON,[3] SEAN MOLESKY,[2] ANDREW IVANOV,[3] KARINE HESTROFFER,[4] FARIBA HATAMI,[4] ALEJANDRO W. RODRIGUEZ,[2] AND KAI-MEI C. FU[1,3]

[1] *Department of Electrical and Computer Engineering, University of Washington, Seattle, Washington 98195, USA*
[2] *Department of Electrical Engineering, Princeton University, Princeton, New Jersey 08544, USA*
[3] *Department of Physics, University of Washington, Seattle, Washington 98195, USA*
[4] *Department of Physics, Humboldt-Universitat zu Berlin, Newtonstrasse, Berlin, Germany*
[5] *e-mail: pengning@princeton.edu*
**Corresponding author: srivatsa@uw.edu*

Received 28 August 2020; revised 21 October 2020; accepted 11 November 2020 (Doc. ID 408611); published 18 December 2020

Solid-state defect qubit systems with spin-photon interfaces show great promise for quantum information and metrology applications. Photon collection efficiency, however, presents a major challenge for defect qubits in high refractive index host materials. Inverse-design optimization of photonic devices enables unprecedented flexibility in tailoring critical parameters of a spin-photon interface including spectral response, photon polarization, and collection mode. Further, the design process can incorporate additional constraints, such as fabrication tolerance and material processing limitations. Here, we design and demonstrate a compact hybrid gallium phosphide on diamond inverse-design planar dielectric structure coupled to single near-surface nitrogen-vacancy centers formed by implantation and annealing. We observe up to a 14-fold broadband enhancement in photon extraction efficiency, in close agreement with simulations. We expect that such inverse-designed devices will enable realization of scalable arrays of single-photon emitters, rapid characterization of new quantum emitters, efficient sensing, and heralded entanglement schemes.

https://doi.org/10.1364/OPTICA.408611

1. INTRODUCTION

Optically addressable defect qubits in materials like diamond [1,2] and silicon carbide [3] are promising for the realization of a wide range of quantum technologies including single-photon generation, quantum metrology, and quantum information protocols [4,5]. In all of these applications, photon collection efficiency is a key figure of merit. The photoluminescence (PL) detection efficiency is intrinsically limited by the non-directional emission of PL and total internal reflection between the high-index host material and its low-index environment. To enable high PL collection efficiency, photonic structures such as solid immersion lenses [6], waveguides [7,8], and microcavities [9–12] have been utilized. Nanophotonic devices are particularly attractive for their small footprint and potential for scalable integration. However, optimizing nanophotonic structures for efficient defect integration is often nontrivial and bespoke due to the unique constraints imposed by the targeted application for a specific defect system. For high-sensitivity quantum metrology with nitrogen vacancy (NV) centers in diamond, photonic structures should be optimized for efficient broadband extraction of PL from NVs located a few nanometers (nm) from the sensing surface. In contrast, for quantum information applications, photonic coupling to the sharp zero-phonon line (ZPL) of deep NV centers (>100 nm from the surface) and operation under the high-cooperativity (Purcell-enhanced) regime is preferable.

Here, we present a flexible inverse-design optimization framework that can reconcile a wide range of design constraints and generate planar dielectric gallium phosphide (GaP)-on-diamond photonic structures. We selected GaP due to its high refractive index ($n = 3.31$) and low loss at the NV emission energy. The structural patterning is constrained to the GaP layer in order to minimize perturbations of the defect environment. For a dipole located 100 nm from the surface and oriented perpendicular to the NV axis, an optimized 1.5 μm × 1.5 μm device is calculated to provide a 15.7-fold PL enhancement of the free-space PL collection. The 100 nm dipole depth corresponds to the surface defect separation, at which NV centers synthesized by implantation and annealing have been shown to exhibit high optical coherence [13]. Orders of magnitude larger enhancement factors are found for devices designed for defects positioned closer to the surface. Recent work [14,15] on fundamental bounds to related design goals such as maximizing scattering cross section or near-field radiation extraction suggest that inverse-designed devices can have performance approaching the absolute theoretical limit.

2334-2536/20/121805-07 Journal © 2020 Optical Society of America

Experimentally, we fabricate the optimized GaP-on-diamond photon extractors and observe efficient PL collection from implanted single NV centers. These versatile devices exhibit a broadband PL enhancement for wavelengths in the measured range of 575 nm to 750 nm with up to a 14-fold ZPL enhancement for single NV centers. Extensive optical characterization of the NV centers performed both before and after fabrication provides insight into changes in the local NV environment. Post-fabrication sample treatment substantially improves device NV optical stability and points to important fabrication/design considerations for future defect qubit-photonics integration.

2. DESIGN OF INVERSE-DESIGNED PHOTON EXTRACTORS

The photon extractors are designed for robust enhancement of ZPL photon collection from near-surface NV centers and modeled via a three-dimensional (3D) finite-difference frequency-domain (FDFD) solver, with the frequency set at the negatively charged NV-ZPL of 637 nm. Topology optimization (TO) [16] was used to design the device within a design region situated directly on top of the diamond substrate with dimensions of 1.5 µm × 1.5 µm × 0.25 µm. A harmonic dipole source representing the NV center is situated 100 nm below the diamond-GaP interface.

The optimization objective for any given dipole polarization is the net Poynting flux through a square collection surface ∂F of sidelength 1.5 µm, situated 0.4 µm above the top surface of the device. To make the device robust with respect to uncertainty in the NV center polarization state, a minimax formulation was used so as to maximize the minimum Poynting flux contribution from dipoles with $\hat{\boldsymbol{x}}$, $\hat{\boldsymbol{y}}$, and $\hat{\boldsymbol{z}}$ polarizations. The optimization problem is formulated as follows:

$$\begin{aligned} &\underset{\epsilon_i}{\text{maximize}} \;\; t \\ &\text{subject to} \;\; t < \min_j \left[\iint_F \mathbf{S}^j \cdot \hat{\mathbf{z}} \mathrm{d}x \mathrm{d}y \right], \\ &\qquad\qquad \epsilon_i \in [1, \epsilon_{\mathrm{GaP}}], \end{aligned} \tag{1}$$

where $\mathbf{S} = \frac{1}{2}\mathrm{Re}\{\mathbf{E}^* \times \mathbf{H}\}$ is the Poynting vector, ϵ_i is the permittivity at the ith location within the design region, and the superscript $j \in [x, y, z]$ runs over different polarizations of the time harmonic dipole source. t is an auxiliary variable representing the minimum of the flux for the different source polarizations, introduced so the optimization objective and constraints are all differentiable with respect to the degree of freedom. In principle, TO allows the relative permittivity of each spatial discretization voxel within the design region to be a degree of freedom; to accommodate fabrication using electron beam lithography, the actual degrees of freedom form a two-dimensional (2D) grid and represent a top-down view of the device. Density and binarization filters [17] were used to restrict the minimum feature size to around 50 nm, well within the capabilities of electron beam lithography. The adjoint method [18,19] is used to efficiently calculate the gradient for the design objective with respect to every degree of freedom.

A schematic representation and xy cross section of the fabricated design are shown in Fig. 1(a) with the fabricated devices shown in Fig. 1(b). Figure 1(c) shows the local density of states (LDOS) and collection flux enhancement spectra of the device for different dipole polarizations, with $\hat{x}$ and $\hat{y}$ polarizations producing nearly the same spectrum due to the resulting near-mirror-device symmetry. A few salient features of the optimized design are worth commenting upon. To begin with, the extractor yields orders of magnitude larger flux enhancements for $\hat{z}$ compared to in-plane polarized dipoles. Such a vast difference in relative improvement follows from the fact that the bulk of the radiation from a $\hat{z}$-polarized dipole underneath a bare diamond-air interface undergoes total internal reflection, suppressing the collection efficiency by more than an order of magnitude compared to that of an in-plane polarized dipole; the main role of the extractor is therefore to out-couple such previously trapped radiation. Further, device performance is robust against spatial displacement of the emitter; the enhancement factor decreases by less than 50% for spatial displacements smaller than 70 nm from the original location of the NV center (see Fig. SI.1, Supplement 1).

Simulating an experimental setup with microscope NA of 0.7, the emitter being an NV center in (100) terminated diamond at a depth of 100 nm coupled to the extractor patterned in GaP (including the resist mask), the fabricated design [Fig. 1(a)] achieves a total collection flux enhancement of 15.7 relative to a bare interface. This is attributed to a 1.4 times LDOS enhancement and an 11 times collection efficiency enhancement [Fig. 1(c)]. For comparison, a full GaP slab with the same thickness as the device achieves a 1.2 times LDOS enhancement but actually reduces collection efficiency by 15%, leading to roughly the same collected flux as that of the bare interface. With regards to the absolute collection efficiency, 1.8% of total NV radiation can be collected from a bare interface, 1.6% collected with a full GaP slab, and 20% collected with the optimized design (Section SI.2, Supplement 1 for simulation details and NV flux enhancement spectrum). For calculations of the far-field radiation pattern of the extractor device see Fig. SI.3, Supplement 1.

While the extractor leads to large enhancements in the total collected flux, it does not significantly increase the net radiation from the NV center, quantified by the LDOS; hence, most of the observed improvement comes from a higher collection efficiency as opposed to fluorescence rate enhancement via the Purcell effect. Figures 1(d) and 1(e) explore this trade-off for a $\hat{z}$-polarized dipole. At each targeted defect depth, we use TO to design two devices, one with LDOS enhancement as the maximization objective and the other with total collected flux enhancement as the maximization objective. For shallow dipoles, optimizing for larger flux (square data points) results in a substantial contribution due to LDOS enhancement. However, the divergence between these two design objectives is observed to grow rapidly with increasing dipole depth: beyond a depth of 75 nm, devices designed to maximize the collected flux maintain a flux enhancement ratio of about 100, while their LDOS enhancement is close to one. Notably, beyond a dipole depth of 150 nm, even LDOS optimized devices are only able to achieve LDOS enhancements of roughly two, as the result of the rapidly decaying access of the device to the dipole's near field. Devices that combine the benefits of Purcell enhancement with increased collection efficiency through interference are therefore only needed for NV centers sufficiently close ($\lesssim$100 nm) to the interface.

Finally, with regards to the device footprint and material choice, we note that for the target emitter depth of 100 nm for the fabricated design, the device footprint of $(1.5\ \mu\mathrm{m})^2$ covers a large effective NA (relative to the dipole), and TO attempts with larger

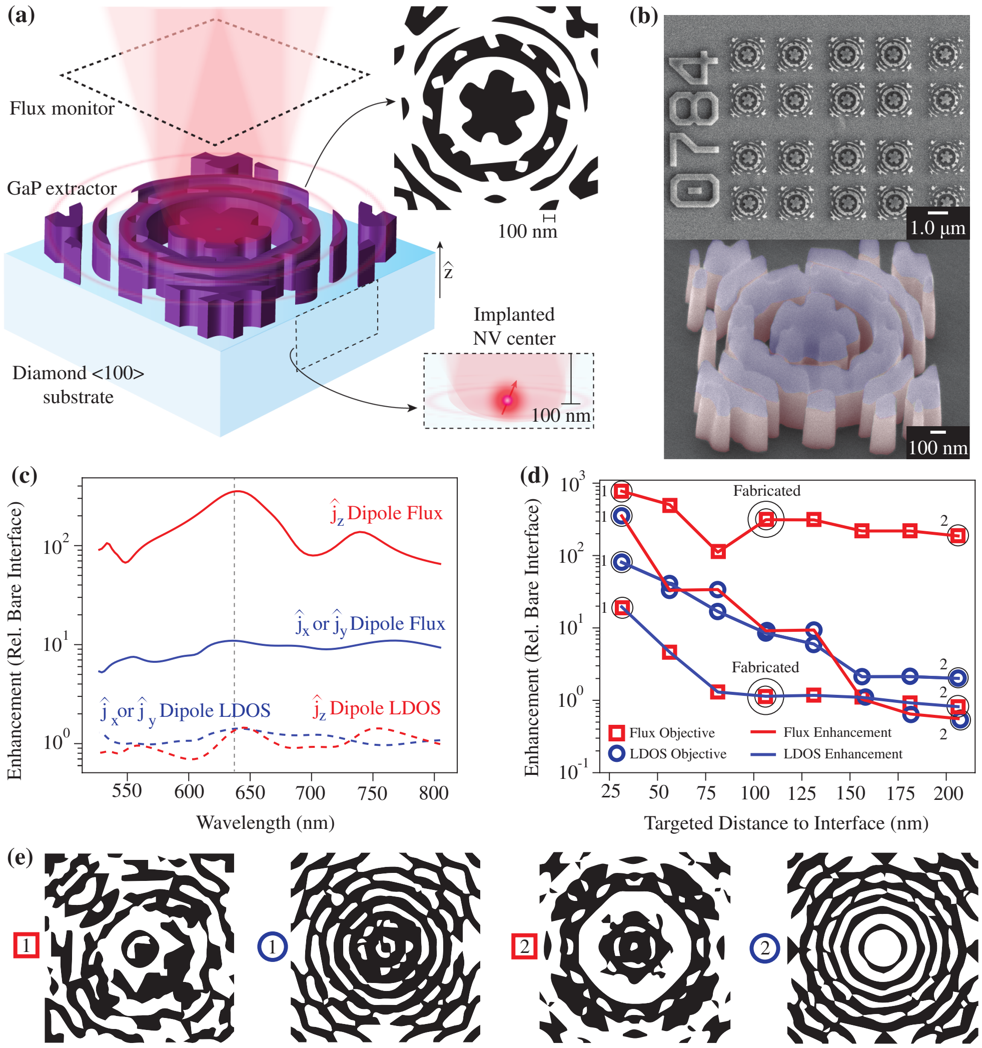

Fig. 1. (a) Schematic of the photon extractor designed via topology optimization (TO). (b) Top: SEM image of an array of fabricated inverse-design extractor structures. Bottom: colorized SEM of a single device indicating the different layers; hydrogen silsesquioxane (HSQ) resist (blue), GaP (pink), and diamond (gray). (c) Spectra of LDOS and collection flux enhancement relative to a bare diamond-air interface. Vertical dotted line indicates NV^- ZPL (637 nm). (d) Performance of TO-designed devices targeting z-polarized dipoles at different depths with either LDOS or collection flux enhancement as the optimization objective. Blue circles are LDOS optimized devices and red squares are flux optimized devices; on the different curves, the same symbols at the same target distance correspond to the same device. (e) Inverse-design structures generated by TO for specific combinations of optimization objective and dipole depth indicated in (d). Around the ZPL, the LDOS optimized structure for dipole depth of 30 nm (1, blue circle) has a dominant mode with $Q = 240$; all of the other structures have an estimated $Q \approx 50$.

device footprints show diminishing increase in device performance. As GaP is a strong dielectric with a high susceptibility, there are limited gains to switching to a higher susceptibility material (Fig. SI.4, Supplement 1), and the low loss of GaP among high-susceptibility materials in this frequency range make it particularly attractive for integrated photonics applications [12].

3. GaP PHOTON EXTRACTORS COUPLED TO IMPLANTED NVs

We fabricate photon extractors [Fig. 1(b)] on two samples, one for ensemble-averaged measurements (Sample A) and the other for single-emitter characterization (Sample B). Sample A is a high-pressure, high-temperature synthesized diamond (Element Six, $N < 200$ ppm, $B < 0.1$ ppm) implanted with ^{14}N accelerated to 20 keV and vacuum annealed at 800°C. Here, annealing forms NVs primarily by vacancy recombination with native nitrogen. The resulting NV distribution is dictated by the vacancy diffusion profile [20], yielding a dense layer (≈ 100 NVs per 800 nm excitation spot diameter) of NV centers $\lesssim 100$ nm below the diamond surface. Sample B is a chemical vapor deposition diamond (Element Six, electronic grade, $N < 5$ ppb, $B < 1$ ppb) implanted with ^{15}N accelerated to 85 keV and vacuum annealed at 1200°C (see Methods). During annealing, NV centers are formed primarily by vacancy recombination with the implanted nitrogen, yielding a thin layer (≈ 3 NVs per excitation spot) of single NV centers 100 nm ± 20 nm from the surface.

After NV formation, a 250 nm thick GaP membrane is transferred to each sample via a wet lift-off process [11,12,21]. Electron beam lithography and subsequent plasma reactive ion etching (RIE) of the GaP layer forms the $1.5\ \mu\text{m} \times 1.5\ \mu\text{m}$ photon extractors. The small footprint was chosen for compatibility with on-chip electrodes enabling optical frequency tuning [12,22]. Over 100,000 devices are fabricated in multiple arrays on the 2 mm × 2 mm diamond substrate. An array of fabricated devices and a false color scanning electron microscope (SEM) image highlighting the material stack is shown in Fig. 1(b). On average, each feature is measured to be within 10% of the design, with near vertical ($\theta = 88°$) GaP sidewalls. See Section SI.5, Supplement 1 for more details on fabrication.

4. RESULTS AND DISCUSSION

A. Enhanced Photon Extraction

To study NV PL enhancement from the fabricated devices, we use spatially resolved PL spectroscopy (Section SI.6, Supplement 1) under off-resonant 532 nm excitation [Fig. 2(a)]. First, Sample A is utilized for broadband characterization of ensemble-averaged enhancement over the entire NV spectrum. In this measurement, the 532 nm laser with a spot diameter of ≈ 800 nm is focused on the center of the device, optimized for maximum PL collection. Due to both the lateral extent of the excitation spot and the depth distribution of the NV ensemble, the NV device coupling is highly inhomogeneous. The room temperature spectra from devices are normalized to the PL from the nearby bare diamond, which spatially varies in intensity by ≈ 14% [Fig. SI.7(b), Supplement 1]. We observe an average six-fold enhancement that is relatively flat over 575 to 750 nm and matches reasonably well to the theoretical four-fold enhancement [Figs. 2(b) and 2(c)] calculated by averaging over the NV spatial and dipole distributions (for details on the simulation see Section SI.2, Supplement 1).

Having demonstrated broadband NV PL enhancement, we move on to single NV-coupled devices on Sample B and characterize the enhancement of the NV ZPL emission. Identification of single NV-coupled devices is performed by comparing the low-temperature (8 K) NV^- ZPL spectra under 532 nm excitation of devices to nearby bare diamond NV centers [Fig. 2(d)]. Enhanced ZPL collection rates [Fig. 2(e)] were exhibited in 74 of 480 tested devices. The distribution of observed enhancement can be seen in Fig. 2(e) (inset). Enhancement as high as 14-fold can be observed, which is based on the NV saturation intensity to eliminate the effect of excitation polarization. The saturation intensity of bare diamond NV centers varies by ≈ 8% [Fig. SI.7(d), Supplement 1]. The placement of NVs with respect to the device optical mode is random; coupled device yield can thus be significantly improved by targeted implantation or pattern alignment to registered defect centers [23] during fabrication.

We verify that the observed enhanced PL emission corresponds to single emitters using an autocorrelation measurement on the NV^- ZPL at 637 nm. Figure 2(f) shows the normalized coincidences under continuous off-resonant excitation for a device-coupled NV. The dip in coincidences at zero time delay is $0.12 < 0.5$ and verifies single-photon emission. Autocorrelation measurements on the eight brightest devices confirm single NV coupling in six of the devices. In addition to the dip at zero time delay, significant bunching is observed in all devices on the 100 ns timescale. In modeling the autocorrelation curve [red line, Fig. 2(f)], we find that it is necessary to include both the NV^- singlet state and the NV^0 charge state to reproduce the magnitude and timescale of the bunching for a series of power-dependent measurements. Consideration of charge-state dynamics is critical for NV device performance, as discussed further below. Consistent with theoretical expectations, a significant excited-state lifetime reduction [due to an increased LDOS, Fig. 1(c), dashed lines] is not necessary to obtain good agreement between the experimental

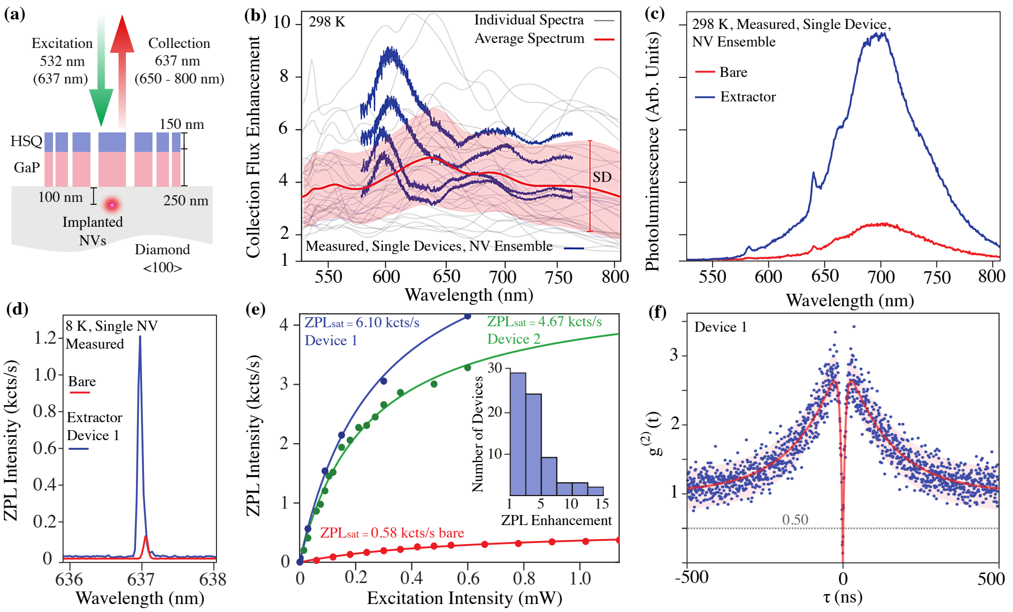

Fig. 2. (a) Illustration of measurement configuration with implanted NV centers coupled to extractor devices. (b) Comparison of simulated (gray) and measured (blue) broadband enhancement for devices coupled to the NV ensemble (Sample A). The red line indicates the average simulated spectrum, and the red envelope is one standard deviation around the average. Variation in individual spectra for both simulation and measurement stems from randomness of NV positions relative to any given device. (c) The broadband PL emission by NV ensemble from an extractor device (blue) versus the bare diamond interface (red). (d) Single NV ZPL emission on sample B from an extractor device (blue) versus the bare diamond interface (red). (e) Saturation count rates from devices coupled to single NV centers. Inset: histogram of measured devices and the observed ZPL enhancement (Sample B). (f) $g^2(\tau)$ measurement of device coupled to single NV (Sample B) under 532 nm 300 μW excitation.

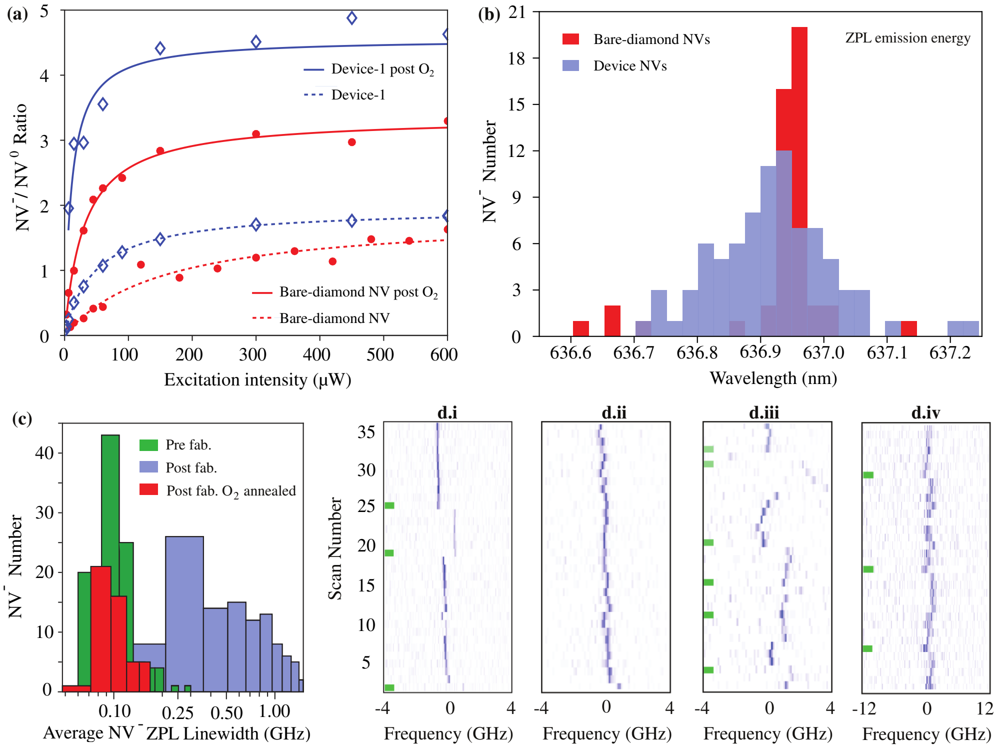

Fig. 3. (Sample B, $T = 8$ K) (a) The ratio of ZPL intensities of NV^- (637 nm) and NV^0 (575 nm) charge states for device-coupled and bare-diamond-implanted NVs as a function of the 532 nm excitation intensity. (b) The distribution of ZPL wavelength for device-coupled and bare diamond NVs. (c) The distribution of observed average PLE linewidth for bare diamond NVs. (d) PLE characterization of NVs; (d.i) Grown-in deep NV average linewidth = 44 MHz, (d.ii) implanted NV pre-fabrication average linewidth = 66 MHz, (d.iii) bare diamond NV post-fabrication after oxygen annealing average linewidth = 59 MHz, (d.iv) device-coupled NV after oxygen annealing average linewidth = 844 MHz. The green markers indicate 532 nm repump pulses that re-initialize the NV into the NV^- charge state.

data and model. Details of the modeling procedure and optimized rates are provided in Section SI.8, Supplement 1.

B. Charge State and Spectral Stability

Single-defect qubit devices have requirements beyond photon collection efficiency, including charge-state stability and spectral homogeneity and stability. These properties should be preserved during device integration. Our autocorrelation model suggests that rapid charge-state conversion occurs between the neutral (NV^0) and negatively charged (NV^-) states. For both sensing and quantum information applications, the NV^- charge state is required, hence we need to minimize ionization into the NV^0 charge state. Every NV center, whether or not it is coupled to a device, has emission at both NV^0 and NV^- ZPL transitions, with the ratio of the ZPL intensities [Fig. 3(a)] determined by the local Fermi-level [24,25] and excitation intensity [26]. We also observe a broadening in the inhomogeneous NV^- ZPL distribution and an overall blue shift of 30 ± 15 GHz [Fig. 3(b)] for device-coupled NVs versus nearby bare diamond NVs. These effects can be attributed to local variation in the strain environment [27,28]. Identical photon emission from different coupled defects are essential for photon-mediated defect qubit entanglement schemes [29,30]. The observed static inhomogeneity can be bridged by Stark tuning [12,22] or quantum frequency conversion techniques [31,32]. Characterization of the local strain environment for individual device-coupled NV centers and the prospect of additional inhomogeneous broadening due to strain induced by the GaP-diamond interface at low temperatures (8 K) is provided in Section SI.9, Supplement 1.

High-resolution PL excitation (PLE) spectroscopy gives us further insight into the optical coherence [Fig. 3(c)] and temporal spectral stability of individual defects [Fig. 3(d)]. In PLE measurements, a narrow-band tunable laser is scanned across the NV^- ZPL while collecting the NV^- phonon sideband PL (650 nm to 800 nm). From the PLE spectra, we obtain the average optical linewidth as well as the scan-to-scan variation in the ZPL frequency, indicating spectral diffusion. During PLE, we can sometimes observe a loss of the NV^- PL signal due to ionization to the NV^0 state. When PL is lost, we apply a short 532 nm repump pulse (0.1 s) between scans to reinitialize into the NV^- charge state [as indicated by the green markers in Fig. 3(d)]. Hence, the interval between repump pulses is another indicator of the NV^- charge-state stability.

For a deep, single NV center incorporated during growth, NV^- is the preferred charge state at low excitation power ($NV^-/NV^0 = 3.4$ at 60 μW of 532 nm excitation). An average linewidth of 44 MHz is observed [Fig. 3(d.i)]. Minimal spectral diffusion is observed between repump pulses, with the NV^- ZPL frequency exhibiting a standard deviation of 48 MHz. It is a challenge to demonstrate this level of optical stability with device-coupled implanted near-surface NVs. Prior to device fabrication, the implanted single NV centers exhibit an average optical linewidth of < 100 MHz [Fig. 3(c), green]. Between repump pulses, the standard deviation of the NV^- ZPL frequency is ∼100 MHz, indicating low spectral diffusion [Fig. 3(d.ii)]. The

NV^- charge state remains stable, and no ionization is observed for multiple scans over 10 min of measurement time. This data compares favorably with the grown-in NVs.

Post-fabrication, for both device and bare-diamond-implanted NV centers, the preferred charge state at low excitation power is NV^0. In addition to the low NV^-/NV^0 ratio [Fig. 3(a) dashed lines], we observe broadening of the average single NV^- linewidth [Fig. 3(c), blue], rapid ionization, and large spectral diffusion. We suspect that although our design avoids etching into the diamond, the GaP photonics plasma etch ($Ar/Cl_2/N_2$) modifies the surface termination [33,34] of the diamond and introduces new surface charge traps. Encouraged by prior studies [24,35], we performed a post-fabrication oxygen anneal of the sample at 400°C (for details see Section SI.10, Supplement 1). From Fig. 3(a) (solid lines), we see that the surface treatment more than doubles the NV^-/NV^0 ratio. For the bare diamond NV centers, we recover the pre-fabrication average NV^- linewidth [Fig. 3(c), red], but the centers retain the larger spectral diffusion [Fig. 3(d.iii)]. For device-coupled NV centers [Fig. 3(d.iV)], we measure an average device-coupled NV linewidth of 844 MHz (1.5 GHz pre-O_2 annealing). This linewidth is ≈ 8 times larger than bare diamond NVs. Further studies are needed to determine if this fast spectral diffusion can be attributed to the GaP-diamond interface or is laser-induced due to modification of the excitation intensity profile. One promising avenue for further reduction in fabrication-induced NV instability is to fabricate the GaP device prior and transfer it via a stamping process [36]. Our inverse-design optimization framework can accommodate additional constraints such as interconnected support structures required by the stamp-transfer fabrication technique.

5. CONCLUSION

This work utilizes inverse-design techniques to optimize the photon collection efficiency from single NV centers under three conditions chosen for future scalability: (1) the NV center is created via implantation, 100 nm from the surface; (2) the diamond defect qubit host is not etched; and (3) the device lateral dimensions are 1.5 µm. Despite these constraints, the resulting 14-fold enhancement performs similar to related broadband devices in the literature (6 to 20-fold enhancement) such as solid immersion lenses [6,37], diamond nanowires [38], bullseye gratings [39], diamond metalenses [40], and parabolic reflectors [41], all of which require directly etching the diamond via harsh processes that degrade near-surface NV optical properties [42]. Other designs based on hybrid metal-dielectric gratings/plasmonic resonances may achieve Purcell enhancement along with high directionality (up to 15-fold enhancement), but they require the NV to be either very close (few nm) to the surface [43] or embedded in the device within a nanodiamond [44–46]; both are extremely challenging environments for the realization of high charge stability and spectral purity required for quantum information applications. We focused on 100-nm-deep centers due to the ability create optically coherent centers at this depth [13]; however, due to the (relatively) large depth, the resulting design predominantly works as a photon extractor with little emission (LDOS) enhancement. As near-surface defect qubit engineering advances, our inverse-design platform can readily be used for even higher enhancement of photon emission from shallower defects. Moreover, the platform provides the design flexibility for integration with emerging technologies such as stamp-transferred devices [36] that can eliminate NV exposure to nearly all fabrication processes to further preserve defect qubit coherence.

During the preparation of this manuscript, we were made aware of a contemporaneous theoretical proposal by Wambold *et al*. [47]. We see the two schemes as complementary, both showcasing the ability of nanophotonic inverse design for handling non-trivial design objectives and constraints. Our design is geared towards quantum information applications, while Wambold *et al.* is focused on quantum metrology.

Funding. National Science Foundation (ECCS-1807566, EFMA-1640986, NNCI-0335765, NNCI-1337840, NNCI-1542101).

Acknowledgment. The photonic devices were fabricated at the Washington Nanofabrication Facility, a National Nanotechnology Coordinated Infrastructure (NNCI) site at the University of Washington, which is supported in part by funds from the NSF. We thank E.R. Schmidgall for help with the fabrication process development and pre-implantation etching of our diamond samples.

Disclosures. The authors declare no conflicts of interest.

See Supplement 1 for supporting content.

[†] These authors contributed equally to this paper.

REFERENCES

1. F. Jelezko and J. Wrachtrup, “Single defect centres in diamond: a review,” Phys. Status Solidi A **203**, 3207–3225 (2006).
2. C. Bradac, W. Gao, J. Forneris, M. E. Trusheim, and I. Aharonovich, “Quantum nanophotonics with group IV defects in diamond,” Nat. Commun. **10**, 5625 (2019).
3. W. F. Koehl, B. B. Buckley, F. J. Heremans, G. Calusine, and D. D. Awschalom, “Room temperature coherent control of defect spin qubits in silicon carbide,” Nature **479**, 84–87 (2011).
4. S. C. Benjamin, D. E. Browne, J. Fitzsimons, and J. J. L. Morton, “Brokered graph-state quantum computation,” New J. Phys. **8**, 141 (2006).
5. R. Raussendorf and H. J. Briegel, “A one-way quantum computer,” Phys. Rev. Lett. **86**, 5188–5191 (2001).
6. M. Jamali, I. Gerhardt, M. Rezai, K. Frenner, H. Fedder, and J. Wrachtrup, “Microscopic diamond solid-immersion-lenses fabricated around single defect centers by focused ion beam milling,” Rev. Sci. Instrum. **85**, 123703 (2014).
7. S. A. Momenzadeh, R. J. Stöhr, F. F. de Oliveira, A. Brunner, A. Denisenko, S. Yang, F. Reinhard, and J. Wrachtrup, “Nanoengineered diamond waveguide as a robust bright platform for nanomagnetometry using shallow nitrogen vacancy centers,” Nano Lett. **15**, 165–169 (2015).
8. M. Radulaski, M. Widmann, M. Niethammer, J. L. Zhang, S.-Y. Lee, T. Rendler, K. G. Lagoudakis, N. T. Son, E. Janzén, T. Ohshima, J. Wrachtrup, and J. Vučković, “Scalable quantum photonics with single color centers in silicon carbide,” Nano Lett. **17**, 1782–1786 (2017).
9. L. Li, T. Schröder, E. H. Chen, M. Walsh, I. Bayn, J. Goldstein, O. Gaathon, M. E. Trusheim, M. Lu, J. Mower, M. Cotlet, M. L. Markham, D. J. Twitchen, and D. Englund, “Coherent spin control of a nanocavity-enhanced qubit in diamond,” Nat. Commun. **6**, 6173 (2015).
10. C. Santori, P. E. Barclay, K.-M. C. Fu, R. G. Beausoleil, S. Spillane, and M. Fisch, “Nanophotonics for quantum optics using nitrogen-vacancy centers in diamond,” Nanotechnology **21**, 274008 (2010).

11. M. Gould, E. R. Schmidgall, S. Dadgostar, F. Hatami, and K.-M. C. Fu, "Efficient extraction of zero-phonon-line photons from single nitrogen-vacancy centers in an integrated GaP-on-diamond platform," Phys. Rev. Appl. **6**, 011001 (2016).
12. E. R. Schmidgall, S. Chakravarthi, M. Gould, I. R. Christen, K. Hestroffer, F. Hatami, and K.-M. C. Fu, "Frequency control of single quantum emitters in integrated photonic circuits," Nano Lett. **18**, 1175–1179 (2018).
13. Y. Chu, N. de Leon, B. Shields, B. Hausmann, R. Evans, E. Togan, M. J. Burek, M. Markham, A. Stacey, A. Zibrov, A. Yacoby, D. Twitchen, M. Loncar, H. Park, P. Maletinsky, and M. Lukin, "Coherent optical transitions in implanted nitrogen vacancy centers," Nano Lett. **14**, 1982–1986 (2014).
14. S. Molesky, P. Chao, W. Jin, and A. W. Rodriguez, "Global T operator bounds on electromagnetic scattering: upper bounds on far-field cross sections," Phys. Rev. Res. **2**, 033172 (2020).
15. S. Molesky, P. Chao, W. Jin, and A. W. Rodriguez, "Global T operator bounds on electromagnetic scattering: upper bounds on far-field cross sections," Phys. Rev. Res. **2**, 033172 (2020).
16. S. Molesky, Z. Lin, A. Y. Piggott, W. Jin, J. Vučković, and A. W. Rodriguez, "Inverse design in nanophotonics," Nat. Photonics **12**, 659–670 (2018).
17. O. Sigmund, "Morphology-based black and white filters for topology optimization," Struct. Multidiscip. Optim. **33**, 401–424 (2007).
18. M. B. Giles and N. A. Pierce, "An introduction to the adjoint approach to design," Flow, Turbul. Combust. **65**, 393–415 (2000).
19. C. M. Lalau-Keraly, S. Bhargava, O. D. Miller, and E. Yablonovitch, "Adjoint shape optimization applied to electromagnetic design," Opt. Express **21**, 21693–21701 (2013).
20. C. Santori, P. E. Barclay, K.-M. C. Fu, and R. G. Beausoleil, "Vertical distribution of nitrogen-vacancy centers in diamond formed by ion implantation and annealing," Phys. Rev. B **79**, 125313 (2009).
21. E. Yablonovitch, D. M. Hwang, T. J. Gmitter, L. T. Florez, and J. P. Harbison, "Van der Waals bonding of GaAs epitaxial liftoff films onto arbitrary substrates," Appl. Phys. Lett. **56**, 2419–2421 (1990).
22. V. M. Acosta, C. Santori, A. Faraon, Z. Huang, K.-M. C. Fu, A. Stacey, D. A. Simpson, K. Ganesan, S. Tomljenovic-Hanic, A. D. Greentree, S. Prawer, and R. G. Beausoleil, "Dynamic stabilization of the optical resonances of single nitrogen-vacancy centers in diamond," Phys. Rev. Lett. **108**, 206401 (2012).
23. L. Marseglia, J. P. Hadden, A. C. Stanley-Clarke, J. P. Harrison, B. Patton, Y.-L. D. Ho, B. Naydenov, F. Jelezko, J. Meijer, P. R. Dolan, J. M. Smith, J. G. Rarity, and J. L. O'Brien, "Nanofabricated solid immersion lenses registered to single emitters in diamond," Appl. Phys. Lett. **98**, 133107 (2011).
24. K.-M. C. Fu, C. Santori, P. E. Barclay, and R. G. Beausoleil, "Conversion of neutral nitrogen-vacancy centers to negatively charged nitrogen-vacancy centers through selective oxidation," Appl. Phys. Lett. **96**, 121907 (2010).
25. H. Kato, M. Wolfer, C. Schreyvogel, M. Kunzer, W. Müller-Sebert, H. Obloh, S. Yamasaki, and C. Nebel, "Tunable light emission from nitrogen-vacancy centers in single crystal diamond PIN diodes," Appl. Phys. Lett. **102**, 151101 (2013).
26. P. Siyushev, H. Pinto, M. Vörös, A. Gali, F. Jelezko, and J. Wrachtrup, "Optically controlled switching of the charge state of a single nitrogen-vacancy center in diamond at cryogenic temperatures," Phys. Rev. Lett. **110**, 167402 (2013).
27. A. Batalov, V. Jacques, F. Kaiser, P. Siyushev, P. Neumann, L. J. Rogers, R. L. McMurtrie, N. B. Manson, F. Jelezko, and J. Wrachtrup, "Low temperature studies of the excited-state structure of negatively charged nitrogen-vacancy color centers in diamond," Phys. Rev. Lett. **102**, 195506 (2009).
28. S. Knauer, J. P. Hadden, and J. G. Rarity, "In-situ measurements of fabrication induced strain in diamond photonic-structures using intrinsic colour centres," npj Quantum Inf. **6**, 50 (2020).
29. H. Bernien, L. Childress, L. Robledo, M. Markham, D. Twitchen, and R. Hanson, "Two-photon quantum interference from separate nitrogen vacancy centers in diamond," Phys. Rev. Lett. **108**, 043604 (2012).
30. P. C. Humphreys, N. Kalb, J. P. J. Morits, R. N. Schouten, R. F. L. Vermeulen, D. J. Twitchen, M. Markham, and R. Hanson, "Deterministic delivery of remote entanglement on a quantum network," Nature **558**, 268–273 (2018).
31. H. Takesue, "Erasing distinguishability using quantum frequency up-conversion," Phys. Rev. Lett. **101**, 173901 (2008).
32. L. Fan, C.-L. Zou, M. Poot, R. Cheng, X. Guo, X. Han, and H. X. Tang, "Integrated optomechanical single-photon frequency shifter," Nat. Photonics **10**, 766–770 (2016).
33. C. J. Widmann, C. Giese, M. Wolfer, S. Kono, and C. E. Nebel, "F- and Cl-terminations of (100)-oriented single crystalline diamond," Phys. Status Solidi A **211**, 2328–2332 (2014).
34. Y. Tao, J. M. Boss, B. A. Moores, and C. L. Degen, "Single-crystal diamond nanomechanical resonators with quality factors exceeding one million," Nat. Commun. **5**, 3638 (2014).
35. H. Yamano, S. Kawai, K. Kato, T. Kageura, M. Inaba, T. Okada, I. Higashimata, M. Haruyama, T. Tanii, K. Yamada, S. Onoda, W. Kada, O. Hanaizumi, T. Teraji, J. Isoya, and H. Kawarada, "Charge state stabilization of shallow nitrogen vacancy centers in diamond by oxygen surface modification," Jpn. J. Appl. Phys. **56**, 04CK08 (2017).
36. A. Dibos, M. Raha, C. Phenicie, and J. Thompson, "Atomic source of single photons in the telecom band," Phys. Rev. Lett. **120**, 243601 (2018).
37. J. P. Hadden, J. P. Harrison, A. C. Stanley-Clarke, L. Marseglia, Y.-L. D. Ho, B. R. Patton, J. L. O'Brien, and J. G. Rarity, "Strongly enhanced photon collection from diamond defect centres under micro-fabricated integrated solid immersion lenses," Appl. Phys. Lett. **97**, 241901 (2010).
38. T. M. Babinec, B. J. M. Hausmann, M. Khan, Y. Zhang, J. R. Maze, P. R. Hemmer, and M. Loncar, "A diamond nanowire single-photon source," Nat. Nanotechnology **5**, 195–199 (2010).
39. L. Li, E. H. Chen, J. Zheng, S. L. Mouradian, F. Dolde, T. Schröder, S. Karaveli, M. L. Markham, D. J. Twitchen, and D. Englund, "Efficient photon collection from a nitrogen vacancy center in a circular bullseye grating," Nano Lett. **15**, 1493–1497 (2015).
40. T.-Y. Huang, R. R. Grote, S. A. Mann, D. A. Hopper, A. L. Exarhos, G. G. Lopez, G. R. Kaighn, E. C. Garnett, and L. C. Bassett, "A monolithic immersion metalens for imaging solid-state quantum emitters," Nat. Commun. **10**, 2392 (2019).
41. N. H. Wan, B. J. Shields, D. Kim, S. Mouradian, B. Lienhard, M. Walsh, H. Bakhru, T. Schröder, and D. Englund, "Efficient extraction of light from a nitrogen-vacancy center in a diamond parabolic reflector," Nano Lett. **18**, 2787–2793 (2018).
42. M. Ruf, M. Jspeert, S. van Dam, N. de Jong, H. van den Berg, G. Evers, and R. Hanson, "Optically coherent nitrogen-vacancy centers in micrometer-thin etched diamond membranes," Nano Lett. **19**, 3987–3992 (2019).
43. A. Karamlou, M. E. Trusheim, and D. Englund, "Metal-dielectric antennas for efficient photon collection from diamond color centers," Opt. Express **26**, 3341–3352 (2018).
44. J. T. Choy, B. J. M. Hausmann, T. M. Babinec, I. Bulu, M. Khan, P. Maletinsky, A. Yacoby, and M. Loncar, "Enhanced single-photon emission from a diamond-silver aperture," Nat. Photonics **5**, 738–743 (2011).
45. N. Livneh, M. G. Harats, D. Istrati, H. S. Eisenberg, and R. Rapaport, "Highly directional room-temperature single photon device," Nano Lett. **16**, 2527–2532 (2016).
46. S. K. H. Andersen, S. Bogdanov, O. Makarova, Y. Xuan, M. Y. Shalaginov, A. Boltasseva, S. I. Bozhevolnyi, and V. M. Shalaev, "Hybrid plasmonic bullseye antennas for efficient photon collection," ACS Photon. **5**, 692–698 (2018).
47. R. A. Wambold, Z. Yu, Y. Xiao, B. F. Bachman, G. R. Jaffe, S. Kolkowitz, J. T. Choy, M. A. Eriksson, R. J. Hamers, and M. A. Kats, "Adjoint-optimized nanoscale light extractor for enhanced luminescence from color centers in diamond," in *2020 IEEE Research and Applications of Photonics in Defense Conference (RAPID)* (IEEE, 2020).